

Ferromagnetic semimetal and charge-density wave phases of interacting electrons in a honeycomb moiré potential

Yubo Yang,¹ Miguel A. Morales,¹ and Shiwei Zhang¹

¹Center for Computational Quantum Physics, Flatiron Institute, New York, NY, 10010, USA

(Dated: June 5, 2024)

The exploration of quantum phases in moiré systems has drawn intense experimental and theoretical efforts. The realization of honeycomb symmetry has been a recent focus. The combination of strong interaction and honeycomb symmetry can lead to exotic electronic states such as fractional Chern insulator, unconventional superconductor, and quantum spin liquid. Accurate computations in such systems, with reliable treatment of strong long-ranged Coulomb interaction and approaching the large system sizes to extract thermodynamic phases, are mostly missing. We study the two-dimensional electron gas on a honeycomb moiré lattice at quarter filling, using fixed-phase diffusion Monte Carlo. The ground state phases of this important model are determined in the parameter regime relevant to current experiments. With increasing moiré potential, the systems transitions from a paramagnetic metal to an itinerant ferromagnetic semimetal and then a charge-density-wave insulator.

Introduction.— When two monolayers of crystalline patterns are stacked with a small misalignment, their interference creates a moiré superlattice with long wavelength. This allows the long-range Coulomb interaction to dominate when a dilute gas of carriers is doped into the bilayer. Recently, transition metal dichalcogenide (TMD) devices have become highly productive quantum simulators of strongly interacting physics [1, 2]. Many exotic electronic phases have been realized, including generalized Wigner crystal (GWC) [3–8], Kondo heavy fermion liquid [9, 10], kinetic magnetism [11, 12], fractional Chern insulator [13–15], and unconventional superconductor [16].

Charge carriers injected into a semiconductor heterostructure are well described by a two-dimensional electron gas (2DEG) [17]. Recent realization of the 2DEG in thin semiconductors include ZnO heterostructure [18], AlAs quantum well [19–21], and MoSe₂ [22–24]. Inter-layer coupling in a bilayer TMD device varies in the moiré unit cell and effectively imposes an external periodic potential on the 2DEG. Given the triangular symmetry of the TMD monolayers, the external moiré potential typically shares the triangular (C_3) symmetry of the underlying atomic lattice. However, in special cases, honeycomb (C_6) symmetry can emerge.

The possibility of realizing honeycomb lattices has been a focus of recent studies [25–28]. At the moiré length scale, the emergent Dirac band crossings at the K points can be modified by the Coulomb interaction and give rise to interesting physics. At fractional filling of the honeycomb lattice, long-range interaction is crucial for understanding the GWC phases that arise in the strongly interacting limit. The relative strength of long- and short-range interactions was shown to change the nature of the magnetic interaction from ferromagnetic to anti-ferromagnetic [27]. Experimental efforts have been rapidly advancing in this direction. For example, a switchable ferromagnetic state [29] along with

a fractional Chern insulator [13] were realized in twisted bilayer MoTe₂ devices, while superconductivity was very recently reported in twisted bilayer WSe₂ [16].

In these systems, the rich set of candidate ground states arise from delicate competition and cooperation between band structure, moiré potential, and the interaction. Treating such a correlated electron system is intrinsically hard, and remains an outstanding general problem. It is challenging for theoretical tools to have both high accuracy and low computational scaling, which are often needed to resolve the relative stability among the different candidate orders or phases to give reliable predictions. As we have seen from even the simplest examples of correlated systems such as the Hubbard model [30–32], accurate computational results are indispensable, for benchmarking simpler methods, validating and enhancing theoretical understanding, and making connections with experiments.

In this paper, we study the effect of a moiré potential with honeycomb symmetry on the 2DEG in the presence of strong electron-electron Coulomb interaction. We employ the diffusion Monte Carlo (DMC) method to accurately treat the moiré continuum model. The results from this correlated many-body method are beyond the reach of independent-electron approaches and have not been quantified or observed in this system. We find a rich ground-state phase diagram at quarter filling, including a transition from a paramagnetic metal into a ferromagnetic semimetal phase, before a transition into a GWC, an insulating ferromagnetic charge-density wave state.

Model and Methods.— The moiré continuum hamiltonian [33, 34] (using the Wigner Seitz radius a as length unit and kinetic energy scale $W = \frac{\hbar^2}{2ma^2}$ as energy unit)

$$\mathcal{H} = -\frac{1}{2} \sum_i \nabla_i^2 - \lambda \sum_i \Lambda(\mathbf{r}_i) + r_s \sum_{i<j} \frac{1}{|\mathbf{r}_i - \mathbf{r}_j|} \quad (1)$$

describes a 2DEG with interaction strength $r_s = a/a_B$ in an external moiré potential with depth $\lambda = V_M/W$. The

Bohr radius a_B is set by the effective mass of the electrons m and a dielectric constant. We use the leading-order approximation to the moiré potential in reciprocal space $\Lambda(\mathbf{r}) = \sum_{j=1}^3 2 \cos(\mathbf{r} \cdot \mathbf{g}_j + \phi)$, where \mathbf{g}_j are three of the smallest non-zero reciprocal lattice vectors of the moiré unit cell. The shape of the moiré potential is controlled by a single parameter ϕ . Honeycomb symmetry can be obtained at $\phi = 60^\circ + 120^\circ m$, $m \in \mathcal{Z}$.

We use fixed-phase diffusion Monte Carlo (FP-DMC) to find the ground-state of eq. (1). Details of the methodology are available in Refs. [35–37]. We emphasize that FP-DMC is variational and works directly in the complete-basis-set limit. This approach has been the computational method of choice in the electron gas [38–40], and has demonstrated excellent accuracy in related systems [41]. The method can be applied in the continuum with hundreds of electrons, so we can reach large simulation cells when calculating properties, and draw conclusions more reliably about the thermodynamic limit.

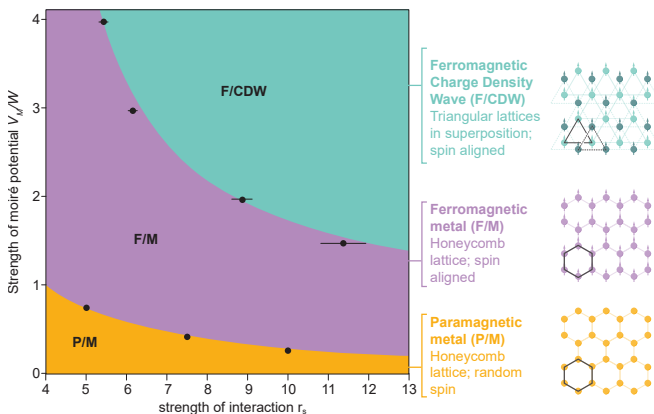


FIG. 1. Ground-state phase diagram of the honeycomb moiré continuum hamiltonian at quarter filling (one electron per moiré unit cell). As the moiré potential and the electron interaction strengths increase, the system exhibits, progressively, three distinct phases: a paramagnetic metal (P/M), a ferromagnetic metal (F/M), and a ferromagnetic insulator with charge density wave order (F/CDW), as illustrated by the cartoons. Black symbols are transition points determined by our QMC calculations.

Results and Discussions.— In the absence of a moiré potential, even under strong Coulomb interaction (e.g., $r_s \sim 30$), the 2DEG is expected to remain a paramagnetic liquid [40]. Therefore, in the experimentally relevant range $5 < r_s < 15$, an external potential is needed to induce long-range charge and magnetic correlations. In the presence of a triangular moiré potential with commensurate wavelength, a GWC is expected to be stable [41]. However, the effect of a moiré potential with honeycomb symmetry is more subtle. Figure 1 summarizes our results. With increasing interaction and moiré

potential depth, we find three distinct phases: a paramagnetic metal (P/M), a ferromagnetic semimetal (F/M), and a ferromagnetic charge density wave (F/CDW). Below we quantify and characterize each phase in more detail. As an overview, when the kinetic energy dominates, the P/M phase is almost identical to the unperturbed 2DEG. It is nearly isotropic with only a small density modulation induced by the moiré potential. As the potential deepens, we find an abrupt transition into the F/M phase, where the spins spontaneously polarize and the Fermi surface shrinks to the K points of the Brillouin zone. From the F/M phase, sufficiently strong interaction can set off a triangular charge density wave, which strongly breaks the honeycomb sublattice symmetry in pair correlations. This insulating F/CDW phase is more isotropic than the F/M phase due to the lack of metallic directions. Qualitatively, it can be visualized as the equal superposition of two triangular GWCs pinned to the two different sublattices of the honeycomb as shown by the depiction at the top right of Fig. 1.

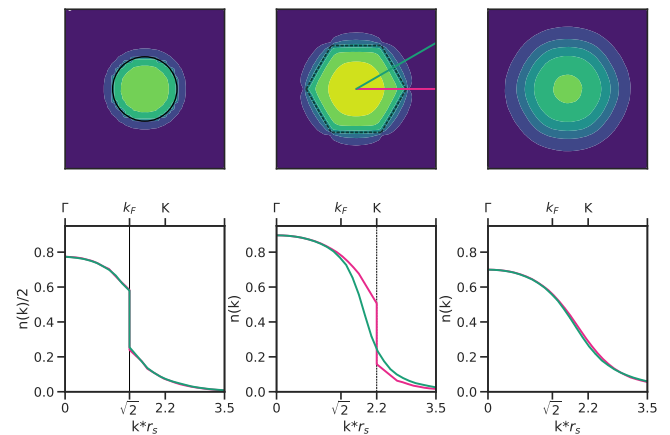


FIG. 2. Momentum distribution at fixed $r_s = 7$ for three representative moiré potential depths: $V_M/W = 0.3, 1,$ and 3 , for the P/M, the F/M, and the F/CDW, respectively. Top panels show 2D density maps, while the bottom panels show 1D linecuts along ΓK (pink) and ΓM (green). Note the nearly isotropic discontinuity in the P/M, the jump at only the K points in the F/M, and the smooth $n(\mathbf{k})$ in the F/CDW insulator.

The three observed phases exhibit distinct signatures in momentum space. Figure 2 shows the momentum distribution $n(\mathbf{k})$ of the three phases. In the P/M phase, $n(\mathbf{k})$ is only weakly perturbed by the moiré potential. The nearly circular Fermi surface remains largely undistorted. Relative to the unperturbed 2DEG (Fig. S1), we find that the moiré potential scatters low-momentum states within the Fermi surface towards secondary Fermi surfaces and the high-momentum tail. In contrast, the response of the ferromagnetic (FM) semimetal to the external potential is highly anisotropic. The Fermi surface is destroyed everywhere except for at the K and K'

points. No secondary Fermi surface is observable along the ΓK and ΓM directions. Compared to the momentum distribution of a polarized Fermi liquid, a substantial and highly anisotropic shift of momentum density can be observed, transitioning from just below k_F to just above k_F . Along ΓM , the redistribution follows a pattern typical of a metal-to-insulator transition, whereas along ΓK , it is more akin to that of a paramagnetic to ferromagnetic metal-to-metal transition. Upon reaching the insulating phase, the Fermi surfaces of the semimetal disappear and $n(\mathbf{k})$ becomes a smooth function.

The metal-insulator transition within the fully polarized sector is subtle. As shown in the top panels of Fig. 3, direct inspection of the one-body density

$$\rho(\mathbf{r}) = N \int d\mathbf{r}_2 \dots d\mathbf{r}_N |\Psi_N(\mathbf{r}, \dots, \mathbf{r}_N)|^2 \quad (2)$$

is not sufficient for identifying the metal-insulator transition from F/M to F/CDW. In an independent-electron solution, for example from Hartree-Fock or a density-functional theory calculation, a CDW phase would break symmetry in the charge density. In the many-body solution, however, the ground-state charge density retains sublattice symmetry on the honeycomb sites in both phases, despite gap openings at the Dirac points in the insulating F/CDW phase. To further characterize and quantify them, we analyze the two-body correlation

$$\rho_2(\mathbf{r}_1, \mathbf{r}_2) = N(N-1) \int d\mathbf{r}_3 \dots d\mathbf{r}_N |\Psi_N(\mathbf{r}_1, \dots, \mathbf{r}_N)|^2. \quad (3)$$

By fixing one of the positions in ρ_2 to the vicinity \mathcal{V} of a particular lattice site, we can examine the charge correlation function with respect to this site. With no loss of generality (due to translational symmetry), we choose a site on the ‘‘B’’ sublattice, \mathbf{R}_B , and compute:

$$\rho_2^B(\mathbf{r}) = \int_{\mathbf{r}_1 \in \mathcal{V}(\mathbf{R}_B)} d\mathbf{r}_1 \rho_2(\mathbf{r}_1, \mathbf{r}_1 + \mathbf{r}), \quad (4)$$

which represents the conditional probability density of finding an electron being at $\mathbf{r} + \mathbf{R}_B$ away, given that site \mathbf{R}_B is occupied. To compare across different phases, we normalize ρ_2^B by the product of the total density on the \mathbf{R}_B site $\rho_B = \int_{\mathbf{r} \in \mathcal{V}(\mathbf{R}_B)} \rho(\mathbf{r}) d\mathbf{r}$ and the mean density ρ_0 . As shown in Fig. 3, $\rho_2^B(\mathbf{r})$ exhibits an exchange-correlation (xc) hole at short distance. The xc hole is of similar shape in all three phases, but is reduced in the P/M because of the presence of opposite spins, and most pronounced in the F/CDW with stronger interaction. In the metallic phases, $\rho_2^B(\mathbf{r})$ retains honeycomb sublattice symmetry away from the xc hole. In the CDW phase, $\rho_2^B(\mathbf{r})$ exhibits long-range periodic structure consistent with a triangular lattice. This is most clearly seen from the tail of the $\rho_2^B(\mathbf{r})$ line cuts in Fig. 3. The imbalance between the BB and BA correlations decay with distance

in the P/M and F/M phases, while the CDW phase has a persistent imbalance.

We can define a measure for the degree of sublattice symmetry breaking using the imbalance in the correlation ρ_2^B at larger distance:

$$S_{AB} = \frac{\rho_2^B(\mathbf{R}_{B_3}) - \rho_2^B(\mathbf{R}_{A_6})}{\rho_2^B(\mathbf{R}_{B_3}) + \rho_2^B(\mathbf{R}_{A_6})}. \quad (5)$$

As labeled in the lower left panel of Fig. 3, the sites \mathbf{R}_{B_3} and \mathbf{R}_{A_6} are the third- and sixth-nearest neighbors of the reference site \mathbf{R}_B on the B and A sublattices, respectively. S_{AB} close to 0 indicates equal occupation of the two sublattices, while S_{AB} close to 1 indicates complete deoccupation of the opposite sublattice. In order to help distinguish metallic and insulating states, we also compute the complex polarization [42, 43]

$$|Z|_N^{\mathbf{g}} = \langle \Psi_N | \exp \left(-i \sum_{j=1}^N \mathbf{g} \cdot \mathbf{r}_j \right) | \Psi_N \rangle, \quad (6)$$

which is related to the degree of electron localization along the $\hat{\mathbf{g}}$ direction, with a value of 0 being delocalized and 1 being highly localized. In the exponent, $\mathbf{g} \cdot \mathbf{r}_j = 2\pi \sum_l m_l s_{jl}$, the vectors \mathbf{m} and \mathbf{s} are fractional coordinates given by $\mathbf{g} = \sum_l m_l \mathbf{b}_l$, $\mathbf{r}_j = \sum_l s_{jl} \mathbf{a}_l$, where \mathbf{a}_l and \mathbf{b}_l are the direct- and reciprocal-lattice vectors of the supercell (sums run over two spatial dimensions). As shown in Fig. 4, both S_{AB} and $|Z|_N^{\mathbf{g}}$ change abruptly across the metal-insulator transition. The absolute magnetization, shown in the top panel of Fig. 4, identifies the ferromagnetic transition at a shallower moiré potential than the metal-insulator transition.

The appearance of large areas of ferromagnetic phases in the honeycomb lattice is in sharp contrast with the triangular case, where only a paramagnetic metal to GWC insulator transition is seen in the moiré continuum Hamiltonian [41]. In general, competing anti-ferromagnetic (AFM) and ferromagnetic (FM) ground states can be stabilized by the moiré potential. The true ground state is determined by a delicate balance between kinetic, moiré, and interaction energies. At a commensurate filling, magnetism induced by the moiré potential is driven by the exchange energy. In this case, the FM phase typically hosts more localized electrons compared to the AFM phase, leading to higher kinetic and lower exchange energy. In a triangular moiré potential [41], this kinetic energy increase overwhelms the gain in exchange energy, leading to an AFM ground state. However, in the honeycomb limit, there are Dirac crossings at the K points in the Brillouin zone when the system is fully polarized. This allows the electrons to delocalize along the ΓK directions, reducing the kinetic energy increase in the FM phase. Further, the more delocalized electrons contribute to lower exchange energy via direct exchange with their nearest neighbors. The F/M phase

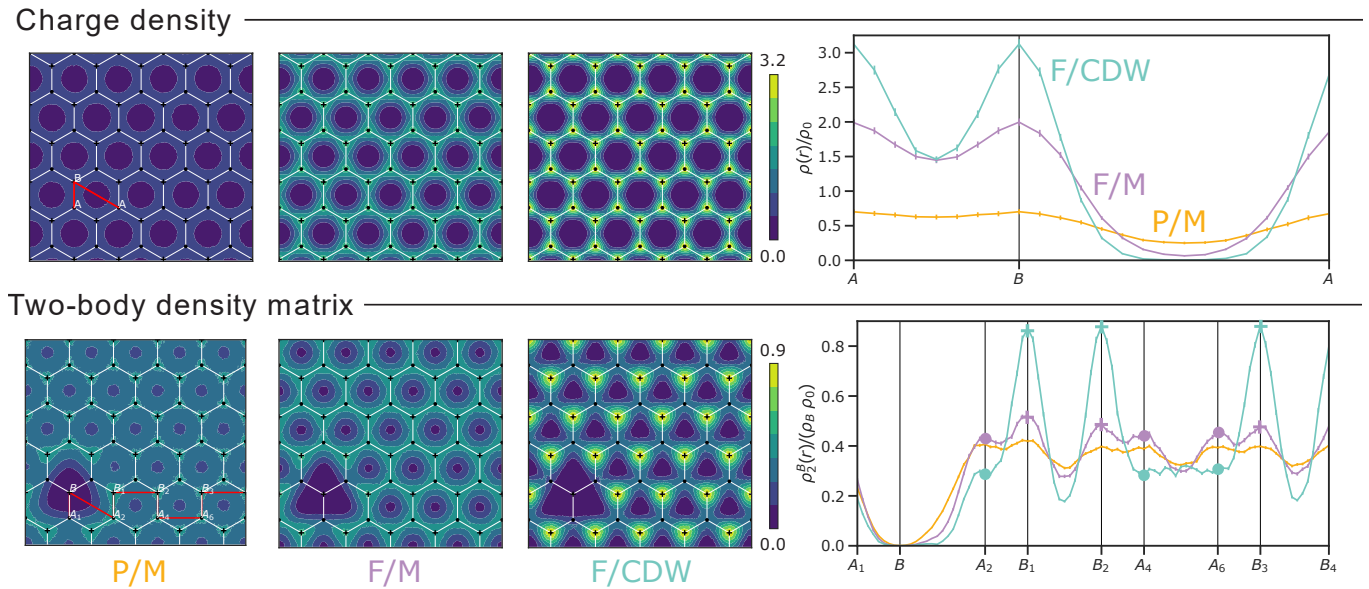


FIG. 3. Charge density (top panels) and the pair distribution function $\rho_2^B(\mathbf{r})$ of eq. (4) (bottom panels) of the three phases at the same conditions as Fig. 2. The charge densities of all three phases show equal occupation of the honeycomb A (black dots) and B (black pluses) sublattices. As quantified by the line cuts, deeper moiré potentials induce stronger density modulations. $\rho_2^B(\mathbf{r})$ exhibits an xc hole around $\mathbf{r} = \mathbf{0}$. Sublattice symmetry is restored away from the hole in the P/M and F/M phases. In the F/CDW phase, strong sublattice symmetry breaking is stable at large separations. To quantify this, $\rho_2^B(\mathbf{r})$ is plotted along the line cut (red line in the bottom left panel) which goes through four pairs of sublattice sites at increasing distances away from the hole. In the P/M phase, no indication of sublattice symmetry breaking can be found away from the xc hole. In the F/M phase, a small amount of sublattice symmetry breaking, which is evident at the nearest-neighbor B_1 site, decays with distance. In the F/CDW phase, strong sublattice symmetry breaking can be observed at all distances.

is robust here but is fragile with respect to variations in the topology. As the moiré potential is tuned away from the honeycomb limit, band gaps open at the Dirac crossings, turning this phase into a band insulator. As the potential is further tuned towards the triangular limit, direct exchange is suppressed and the lowest-energy magnetic order changes from FM to AFM. Detailed analysis of energetic components is provided in the supplemental materials surrounding Fig. S4.

The CDW phase is stabilized by long-range Coulomb interaction, taking place much earlier (at smaller r_s) than in the electron gas due to assistance from the moiré potential. Therefore, it can also be thought of as a GWC phase. The electrons preferentially occupy the same sublattice, as shown by $\rho_2^B(\mathbf{r})$ in Fig. 3. The many-body ground state is an equal superposition of two such states (like a “floating crystal” [44, 45]) which respects the honeycomb symmetry. Once the F/M phase is established, it is perhaps not too surprising to find, upon further increase of the interaction, a transition from the semimetal phase into the CDW phase. The same phenomenon is seen in the spinless fermion model on a honeycomb lattice with near-neighbor interactions, where a number of many-body calculations have established a semimetal to CDW transition for a range of interaction strengths at half-filling [46, 47]. This suggests that, in the moiré systems, the transition we have observed will likely not

be affected by the presence of gates, which screen the Coulomb interaction. It is also an indirect validation that Hubbard-like models (but with at least near-neighbor interactions) could provide a plausible way to qualitatively capture some of the phenomena in these TMD systems.

Conclusion and Outlook.— We have presented a comprehensive analysis of the 2DEG in the presence of a moiré potential with honeycomb symmetry using DMC. With increasing strength of the moiré potential, the system undergoes a paramagnetic-to-ferromagnetic transition where the system remains metallic, followed by a second transition to an insulating charge density wave phase. The F/M phase is characterized by a strongly anisotropic Fermi surface and stabilized by a combination of exchange energy gain and a lower kinetic energy penalty due to the more delocalized nature of electrons in the honeycomb structure. The CDW phase is characterized by a strong sublattice symmetry breaking in pair correlations, leading to a superposition of GWC states with triangular symmetry.

The delicate interplay between band structure, moiré potential, and electron interactions in 2D systems leads to a rich set of interesting ordered states at low temperatures. Accurate many-body approaches are an important for further progress, as models become more complicated and realistic. Quantum Monte Carlo approaches offer an excellent balance between accuracy and scalability, al-

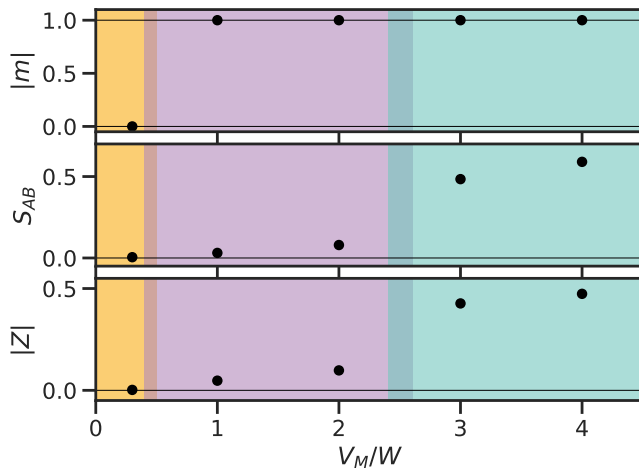


FIG. 4. Quantitative measures of the magnetic and the metal-insulator transitions at $r_s = 7$. $|m|$ is the absolute magnetization per moiré unit cell. S_{AB} measures the degree of sublattice polarization from the two-body density matrix. $|Z|$ is the complex polarization, which measures the degree of electron localization, with 0 being delocalized and 1 being strongly localized. The sudden changes in these quantities identify the transitions among the three phases, which demonstrate magnetic and charge orders consistent with the phase diagram.

lowing continuum models to be treated without further approximations while reaching sufficiently large system sizes that enable more reliable extrapolation to the thermodynamic limit. A variety of related systems are accessible either directly with our approach or by introducing reasonably straightforward variations. Given the rapid pace at which experiments are progressing we hope this work will help open up more broad applications of accurate many-body computations in this area.

Acknowledgment.— The Flatiron Institute is a division of the Simons Foundation. We thank Daniele Guerci, Giorgio Sangiovanni, Valentin Crepel, Yang Zhang, and Yixiao Chen for useful discussions.

[1] D. M. Kennes, M. Claassen, L. Xian, A. Georges, A. J. Millis, J. Hone, C. R. Dean, D. N. Basov, A. N. Pasupathy, and A. Rubio, *Nature Physics* **17**, 155 (2021).
 [2] K. F. Mak and J. Shan, *Nature Nanotechnology* **17**, 686 (2022).
 [3] L. Wang, E.-M. Shih, A. Ghitto, L. Xian, D. A. Rhodes, C. Tan, M. Claassen, D. M. Kennes, Y. Bai, B. Kim, K. Watanabe, T. Taniguchi, X. Zhu, J. Hone, A. Rubio, A. N. Pasupathy, and C. R. Dean, *Nature Materials* **19**, 861 (2020).
 [4] E. C. Regan, D. Wang, C. Jin, M. I. Bakti Utama, B. Gao, X. Wei, S. Zhao, W. Zhao, Z. Zhang, K. Yumigeta, M. Blei, J. D. Carlström, K. Watanabe, T. Taniguchi, S. Tongay, M. Crommie, A. Zettl, and

F. Wang, *Nature* **579**, 359 (2020).
 [5] S. Shabani, D. Halbertal, W. Wu, M. Chen, S. Liu, J. Hone, W. Yao, D. N. Basov, X. Zhu, and A. N. Pasupathy, *Nature Physics* **17**, 720 (2021).
 [6] H. Li, S. Li, E. C. Regan, D. Wang, W. Zhao, S. Kahn, K. Yumigeta, M. Blei, T. Taniguchi, K. Watanabe, S. Tongay, A. Zettl, M. F. Crommie, and F. Wang, *Nature* **597**, 650 (2021).
 [7] R. Nieken, A. Roche, F. Mahdikhanyarvejahany, T. Taniguchi, K. Watanabe, M. R. Koehler, D. G. Mandrus, J. Schaibley, and B. J. LeRoy, *APL Materials* **10**, 031107 (2022).
 [8] Z. Xiang, H. Li, J. Xiao, M. H. Naik, Z. Ge, Z. He, S. Chen, J. Nie, S. Li, Y. Jiang, R. Sailus, R. Banerjee, T. Taniguchi, K. Watanabe, S. Tongay, S. G. Louie, M. F. Crommie, and F. Wang, *arXiv e-prints*, arXiv:2402.05456 (2024), arXiv:2402.05456 [cond-mat.str-el].
 [9] D. Guerci, J. Wang, J. Zang, J. Cano, J. H. Pixley, and A. Millis, *Science Advances* **9**, eade7701 (2023).
 [10] W. Zhao, B. Shen, Z. Tao, Z. Han, K. Kang, K. Watanabe, T. Taniguchi, K. F. Mak, and J. Shan, *Nature* **616**, 61 (2023).
 [11] Z. Tao, W. Zhao, B. Shen, P. Knüppel, K. Watanabe, T. Taniguchi, J. Shan, and K. F. Mak, “Observation of spin polarons in a frustrated moiré Hubbard system,” (2023).
 [12] L. Ciorciaro, T. Smoleński, I. Morera, N. Kiper, S. Hiestand, M. Kroner, Y. Zhang, K. Watanabe, T. Taniguchi, E. Demler, and A. İmamoglu, *Nature* **623**, 509 (2023).
 [13] J. Cai, E. Anderson, C. Wang, X. Zhang, X. Liu, W. Holtzmann, Y. Zhang, F. Fan, T. Taniguchi, K. Watanabe, Y. Ran, T. Cao, L. Fu, D. Xiao, W. Yao, and X. Xu, *Nature* **622**, 63 (2023).
 [14] Y. Jia, J. Yu, J. Liu, J. Herzog-Arbeitman, Z. Qi, N. Regnault, H. Weng, B. A. Bernevig, and Q. Wu, “Moiré Fractional Chern Insulators I: First-principles calculations and Continuum Models of Twisted Bilayer MoTe₂,” (2023), arxiv:2311.04958 [cond-mat].
 [15] Y. Zeng, Z. Xia, K. Kang, J. Zhu, P. Knüppel, C. Vaswani, K. Watanabe, T. Taniguchi, K. F. Mak, and J. Shan, *Nature* **622**, 69 (2023).
 [16] Y. Xia, Z. Han, K. Watanabe, T. Taniguchi, J. Shan, and K. F. Mak, *arXiv e-prints*, arXiv:2405.14784 (2024), arXiv:2405.14784 [cond-mat.mes-hall].
 [17] T. Ando, A. B. Fowler, and F. Stern, *Rev. Mod. Phys.* **54**, 437 (1982).
 [18] J. Falson, I. Sodemann, B. Skinner, D. Tabrea, Y. Kozuka, A. Tsukazaki, M. Kawasaki, K. Von Klitzing, and J. H. Smet, *Nature Materials* **21**, 311 (2022).
 [19] M. S. Hossain, M. K. Ma, K. A. V. Rosales, Y. J. Chung, L. N. Pfeiffer, K. W. West, K. W. Baldwin, and M. Shayegan, *Proceedings of the National Academy of Sciences* **117**, 32244 (2020).
 [20] Md. S. Hossain, M. K. Ma, K. A. Villegas-Rosales, Y. J. Chung, L. N. Pfeiffer, K. W. West, K. W. Baldwin, and M. Shayegan, *Physical Review Letters* **127**, 116601 (2021).
 [21] Md. S. Hossain, M. K. Ma, K. A. Villegas-Rosales, Y. J. Chung, L. N. Pfeiffer, K. W. West, K. W. Baldwin, and M. Shayegan, *Physical Review Letters* **129**, 036601 (2022).
 [22] T. Smoleński, P. E. Dolgirev, C. Kuhlenkamp, A. Popert, Y. Shimazaki, P. Back, X. Lu, M. Kroner, K. Watanabe,

- T. Taniguchi, I. Esterlis, E. Demler, and A. Imamoglu, *Nature* **595**, 53 (2021).
- [23] Y. Zhou, J. Sung, E. Brutschea, I. Esterlis, Y. Wang, G. Scuri, R. J. Gelly, H. Heo, T. Taniguchi, K. Watanabe, G. Zaránd, M. D. Lukin, P. Kim, E. Demler, and H. Park, *Nature* **595**, 48 (2021).
- [24] J. Sung, J. Wang, I. Esterlis, P. A. Volkov, G. Scuri, Y. Zhou, E. Brutschea, T. Taniguchi, K. Watanabe, Y. Yang, M. A. Morales, S. Zhang, A. J. Millis, M. D. Lukin, P. Kim, E. Demler, and H. Park, arXiv e-prints, arXiv:2311.18069 (2023), arXiv:2311.18069 [cond-mat.str-el].
- [25] M. Angeli and A. H. MacDonald, *Proceedings of the National Academy of Sciences* **118**, e2021826118 (2021).
- [26] M. Angeli, G. R. Schleder, and E. Kaxiras, *Physical Review B* **106**, 235159 (2022).
- [27] N. Kaushal, N. Morales-Durán, A. H. MacDonald, and E. Dagotto, *Communications Physics* **5**, 289 (2022).
- [28] H. Pan, E.-A. Kim, and C.-M. Jian, *Physical Review Research* **5**, 043173 (2023).
- [29] E. Anderson, F.-R. Fan, J. Cai, W. Holtzmann, T. Taniguchi, K. Watanabe, D. Xiao, W. Yao, and X. Xu, *Science* **381**, 325 (2023).
- [30] J. P. F. LeBlanc, A. E. Antipov, F. Becca, I. W. Bulik, G. K.-L. Chan, C.-M. Chung, Y. Deng, M. Ferrero, T. M. Henderson, C. A. Jiménez-Hoyos, E. Kozik, X.-W. Liu, A. J. Millis, N. V. Prokof'ev, M. Qin, G. E. Scuseria, H. Shi, B. V. Svistunov, L. F. Tocchio, I. S. Tupitsyn, S. R. White, S. Zhang, B.-X. Zheng, Z. Zhu, and E. Gull (Simons Collaboration on the Many-Electron Problem), *Phys. Rev. X* **5**, 041041 (2015).
- [31] M. Qin, C.-M. Chung, H. Shi, E. Vitali, C. Hubig, U. Schollwöck, S. R. White, and S. Zhang (Simons Collaboration on the Many-Electron Problem), *Phys. Rev. X* **10**, 031016 (2020).
- [32] H. Xu, C.-M. Chung, M. Qin, U. Schollwöck, S. R. White, and S. Zhang, *Science* **384**, eadh7691 (2024), <https://www.science.org/doi/pdf/10.1126/science.adh7691>.
- [33] F. Wu, T. Lovorn, and A. H. MacDonald, *Physical Review B* **97**, 035306 (2018), 1710.10278.
- [34] F. Wu, T. Lovorn, E. Tutuc, and A. H. MacDonald, *Physical Review Letters* **121**, 026402 (2018).
- [35] G. Ortiz, D. M. Ceperley, and R. M. Martin, *Phys. Rev. Lett.* **71**, 2777 (1993).
- [36] W. M. C. Foulkes, L. Mitas, R. J. Needs, and G. Rajagopal, *Rev. Mod. Phys.* **73**, 33 (2001).
- [37] DMC calculations performed using QMCPACK 3.15.9 [48, 49] with appropriate 2D modifications.
- [38] D. M. Ceperley and B. J. Alder, *Physical Review Letters* **45**, 566 (1980).
- [39] C. Attaccalite, S. Moroni, P. Gori-Giorgi, and G. B. Bachelet, *Physical Review Letters* **88**, 256601 (2002).
- [40] N. D. Drummond and R. J. Needs, *Physical Review Letters* **102**, 126402 (2009).
- [41] Y. Yang, M. A. Morales, and S. Zhang, *Physical Review Letters* **132**, 076503 (2024).
- [42] R. Resta and S. Sorella, *Physical Review Letters* **82**, 370 (1999).
- [43] I. Souza, T. Wilkens, and R. M. Martin, *Physical Review B* **62**, 1666 (2000).
- [44] R. F. Bishop and K. H. Lührmann, *Physical Review B* **26**, 5523 (1982).
- [45] M. Lewin, E. H. Lieb, and R. Seiringer, *Physical Review B* **100**, 035127 (2019).
- [46] S. Capponi and A. M. Läuchli, *Physical Review B* **92**, 085146 (2015).
- [47] J. Motruk, A. G. Grushin, F. De Juan, and F. Pollmann, *Physical Review B* **92**, 085147 (2015).
- [48] J. Kim, A. D. Baczewski, T. D. Beaudet, A. Benali, M. C. Bennett, M. A. Berrill, N. S. Blunt, E. J. L. Borda, M. Casula, D. M. Ceperley, S. Chiesa, B. K. Clark, R. C. Clay, K. T. Delaney, M. Dewing, K. P. Esler, H. Hao, O. Heinonen, P. R. C. Kent, J. T. Krogel, I. Kylänpää, Y. W. Li, M. G. Lopez, Y. Luo, F. D. Malone, R. M. Martin, A. Mathuriya, J. McMinis, C. A. Melton, L. Mitas, M. A. Morales, E. Neuscamman, W. D. Parker, S. D. Pineda Flores, N. A. Romero, B. M. Rubenstein, J. A. R. Shea, H. Shin, L. Shulenburger, A. F. Tillack, J. P. Townsend, N. M. Tubman, B. Van Der Goetz, J. E. Vincent, D. C. Yang, Y. Yang, S. Zhang, and L. Zhao, *Journal of Physics: Condensed Matter* **30**, 195901 (2018), 1802.06922.
- [49] P. R. C. Kent, A. Annaberdiev, A. Benali, M. C. Bennett, E. J. Landinez Borda, P. Doak, H. Hao, K. D. Jordan, J. T. Krogel, I. Kylänpää, J. Lee, Y. Luo, F. D. Malone, C. A. Melton, L. Mitas, M. A. Morales, E. Neuscamman, F. A. Reboredo, B. Rubenstein, K. Saritas, S. Upadhyay, G. Wang, S. Zhang, and L. Zhao, *The Journal of Chemical Physics* **152**, 174105 (2020), 2003.01831.

**FERROMAGNETIC SEMIMETAL AND CHARGE DENSITY WAVE PHASES OF INTERACTING
ELECTRONS IN A HONEYCOMB MOIRÉ POTENTIAL : SUPPLEMENTAL MATERIALS**

Momentum Distribution

Figure S1 shows how the moiré potential redistributes the momentum density in the P/M and F/M phases, relative to that of the 2DEG. In the P/M phase, the moiré potential scatters low-momentum states from within the Fermi surface to the high-momentum tail in an isotropic manner, except when close to secondary Fermi surfaces. In contrast, the redistribution of momentum density in the F/M phase near the 2DEG Fermi surface is highly anisotropic. Along the ΓK direction, a similar amount of momentum density is moved across the Fermi surface as in the P/M phase. However, along the ΓM direction, significantly more momentum density is transferred to make $n(k)$ smooth.

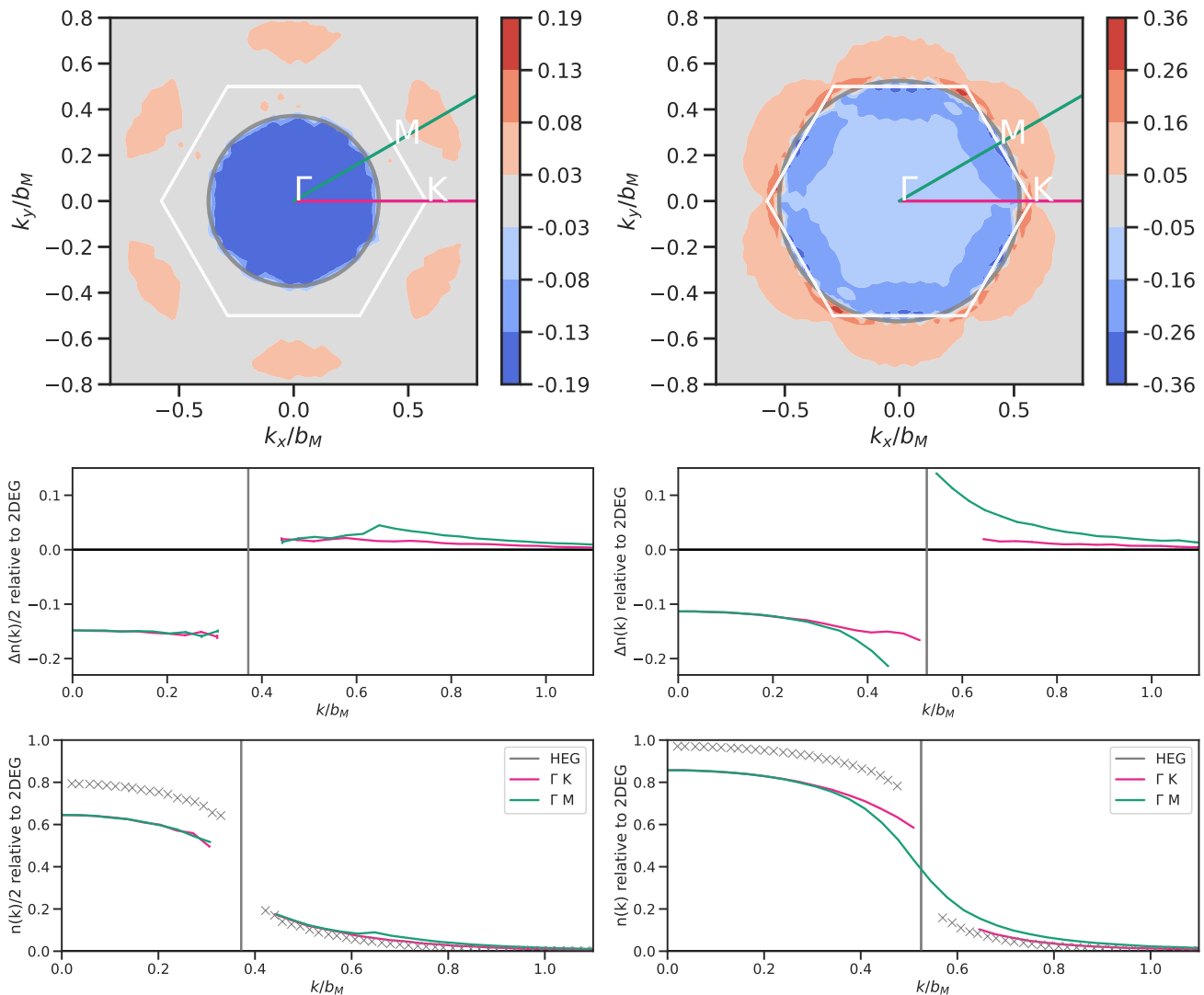


FIG. S1. Redistribution of the electronic momentum density of the two-dimensional electron gas due to the honeycomb moiré potential in the (left) P/M and (right) F/M phases both stabilized at $\lambda = 1.5$. Each simulation contains $N = 144$ electrons with 2×2 twists in the canonical ensemble, which introduces some noise close to the Fermi surface. In the line cuts, points too close to the Fermi surface are excluded.

Determination of Transition Boundaries

The ferromagnetic transition from the P/M to the F/M phase and the metal-insulator transition from the F/M to the F/CDW phase are obtained by comparing total energies of candidate states. We perform meta-stable simulations of the three phases at a range of r_s and $\lambda = V_M/W$ conditions and find the ground state using the variational property of DMC. Non-interacting orbitals are used in the determinant part of the wavefunction for the P/M and F/M phases, whereas Hartree-Fock (HF) orbitals are used for the F/CDW phase. The ferromagnetic transitions are obtained from Fig. S2(a), whereas the metal-insulator transitions are extracted from Fig. S2(b). Twist-averaged DMC total energies are tabulated in Table I. All calculations used to determine the transitions have been performed in simulation cells containing $N = 144$ electrons with 1024 walkers. The total energy is averaged over a shifted uniform grid of twists (2×2) in the canonical ensemble.

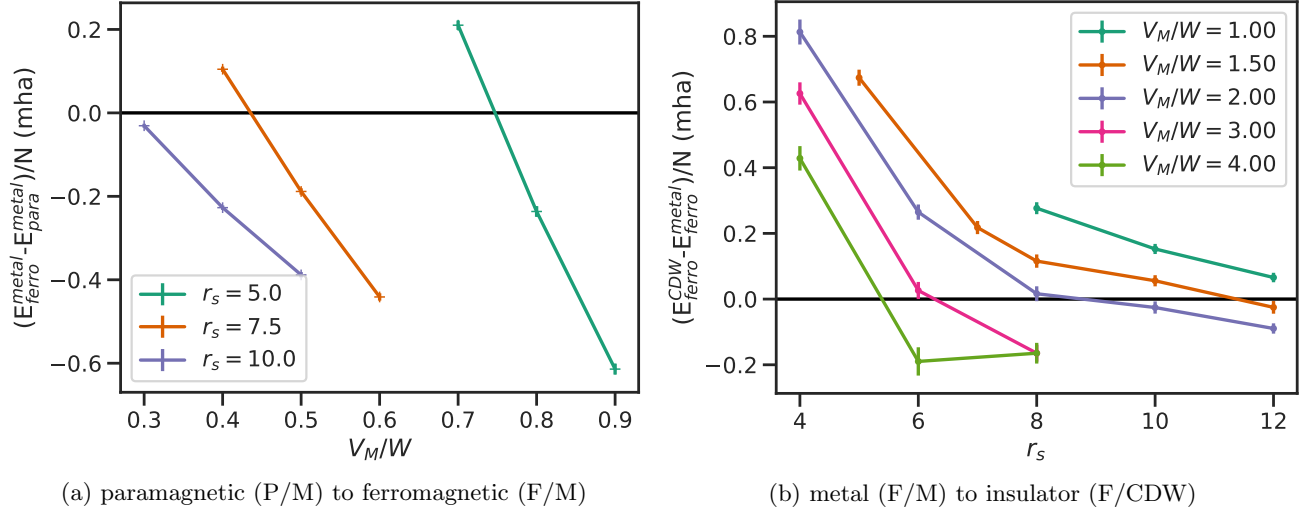


FIG. S2. Transitions determined by total energy difference.

TABLE I. DMC total energies used in Fig. S2.

phase	r_s	λ	E_{tot}	phase	r_s	λ	E_{tot}	phase	r_s	λ	E_{tot}
F/M	5.0	0.7	-0.165712(2)	F/CDW	8.0	1.0	-0.11614(2)	F/CDW	8.0	2.0	-0.13979(2)
P/M	5.0	0.7	-0.16592(1)	F/M	8.0	1.0	-0.116412(5)	F/M	8.0	2.0	-0.13980(2)
F/M	5.0	0.8	-0.170379(2)	F/CDW	10.0	1.0	-0.09429(1)	F/CDW	10.0	2.0	-0.109696(9)
P/M	5.0	0.8	-0.17014(1)	F/M	10.0	1.0	-0.094444(9)	F/M	10.0	2.0	-0.10967(2)
F/M	5.0	0.9	-0.175261(2)	F/CDW	12.0	1.0	-0.07948(1)	F/CDW	12.0	2.0	-0.090353(8)
P/M	5.0	0.9	-0.17465(1)	F/M	12.0	1.0	-0.07954(1)	F/M	12.0	2.0	-0.09026(1)
F/M	7.5	0.4	-0.111334(1)	F/CDW	5.0	1.5	-0.20753(3)	F/CDW	4.0	3.0	-0.41749(3)
P/M	7.5	0.4	-0.111438(6)	F/M	5.0	1.5	-0.208137(4)	F/M	4.0	3.0	-0.418111(8)
F/M	7.5	0.5	-0.113097(2)	F/CDW	8.0	1.5	-0.12742(2)	F/CDW	6.0	3.0	-0.24056(2)
P/M	7.5	0.5	-0.112909(7)	F/M	8.0	1.5	-0.12753(1)	F/M	6.0	3.0	-0.24059(2)
F/M	7.5	0.6	-0.114997(2)	F/CDW	10.0	1.5	-0.10165(1)	F/CDW	8.0	3.0	-0.16689(1)
P/M	7.5	0.6	-0.114555(9)	F/M	10.0	1.5	-0.10171(1)	F/M	8.0	3.0	-0.16672(2)
F/M	10.0	0.3	-0.086346(1)	F/CDW	12.0	1.5	-0.084688(8)	F/CDW	4.0	4.0	-0.53228(3)
P/M	10.0	0.3	-0.086315(5)	F/M	12.0	1.5	-0.08466(2)	F/M	4.0	4.0	-0.53271(1)
F/M	10.0	0.4	-0.087283(1)	F/CDW	4.0	2.0	-0.31168(4)	F/CDW	6.0	4.0	-0.29210(2)
P/M	10.0	0.4	-0.087056(5)	F/M	4.0	2.0	-0.312489(5)	F/M	6.0	4.0	-0.29191(4)
F/M	10.0	0.5	-0.088309(2)	F/CDW	6.0	2.0	-0.19298(2)	F/CDW	8.0	4.0	-0.196124(7)
P/M	10.0	0.5	-0.087920(7)	F/M	6.0	2.0	-0.193249(9)	F/M	8.0	4.0	-0.19596(3)

Superposition of Wavefunctions

The ground state of the F/CDW phase retains honeycomb sublattice symmetry of the Hamiltonian. However, the HF determinant used in our trial wavefunction breaks this symmetry. To restore it for all properties, we use the equal superposition of two HF solutions, one occupying the A sublattice while the other occupying B, in the determinant part of the trial wavefunction

$$\Psi_T = [\Psi_{HF}^A + \Psi_{HF}^B] \exp(-U), \quad (7)$$

where $\exp(-U)$ is the Jastrow. Alternatively, we can restore sublattice symmetry of the density and pair correlation by averaging over elements of the inversion group with generator \mathcal{I} , where $\mathcal{I}\rho(\mathbf{r}) = \rho(-\mathbf{r})$ and $\mathcal{I}\rho_2(\mathbf{r}_1, \mathbf{r}_2) = \rho_2(-\mathbf{r}_1, -\mathbf{r}_2)$. Thus, $\mathcal{I}\rho_2^B(\mathbf{r}) = \rho_2^A(-\mathbf{r})$. The charge density and pair correlation of eq. (4) can be symmetrized as $\rho(\mathbf{r}) \rightarrow [\rho(\mathbf{r}) + \mathcal{I}\rho(\mathbf{r})]/2$ and $\rho_2^B(\mathbf{r}) \rightarrow [\rho_2^B(\mathbf{r}) + \mathcal{I}\rho_2^B(\mathbf{r})]/2$, respectively. As shown in Fig. S3, the two approaches produced identical results at $r_s = 7$ and $V_M/W = 3$. We directly symmetrized the properties shown in Fig. 3.

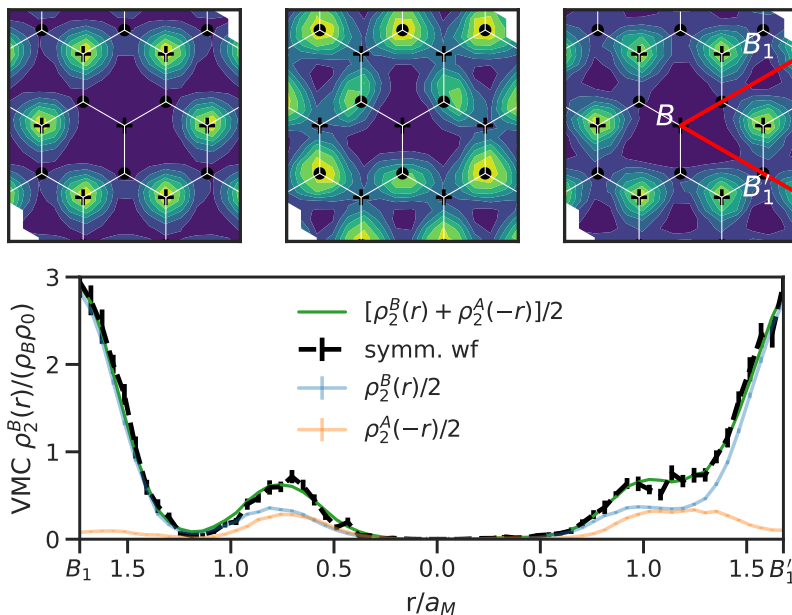


FIG. S3. Symmetrization of pair correlation matches wavefunction superposition at $r_s = 7$ and $V_M/W = 3$. Test calculations were performed with $N = 16$ electron in a simulation cell with periodic boundary conditions.

Comparison with Density Functional Theory

Once the phase diagram Fig. 1 is established by the quantum Monte Carlo calculations, we also attempted to reproduce it using density functional theory. Using LDA, we find the paramagnetic metal to the ferromagnetic semimetal transition, but the band crossings at the K points remain at V_M/W as large as 8. After mixing 50% of exact exchange, we find a direct transition from the paramagnetic metal to the ferromagnetic insulator. We were not able to obtain both the ferromagnetic semimetal and the insulator at any value of exact exchange fraction.

Since the P/M to F/M transition can be captured by DFT calculations using the 2D LDA functional [39], we use it to perform detailed analysis of the band structure and various energy components to help identify the driving mechanism of this transition. We tune the moiré potential from the honeycomb limit ($\phi = 60^\circ$), where we find a ferromagnetic (FM) phase, towards the triangular limit ($\phi = 0^\circ$), where an anti-ferromagnetic (AFM) phase is expected [41]. The charge density, LDA band structure and energy components are shown in Fig. S4. In a honeycomb moiré potential, the LDA band structure always has a band crossing at the K points of the Brillouin zone and a charge density with honeycomb symmetry. However, at $\phi = 46^\circ$, gaps open at the K points and the charge density has only triangular symmetry. Therefore, the honeycomb moiré potential allows the electronic wavefunction to delocalize more uniformly across the two local minima, which enhances the direct exchange interaction. According to the energy components

in Fig. S4, as the system exits the P/M phase around $V_M/W = 0.5$, the FM and AFM phases have nearly identical Hartree energy. The FM phase has lower moiré and exchange-correlation (xc) components than the AFM phase and higher kinetic energy. When the moiré potential has honeycomb symmetry, the kinetic energy of the FM phase is insensitive to its strength (V_M/W). Further, the moiré and xc components are significantly lower than the AFM phase compared to the $\phi = 46^\circ$ case. This together with the changes in the charge density suggest that honeycomb moiré potential favors FM by strengthening the exchange interaction and better utilizing the moiré potential at reduced cost to the kinetic energy.

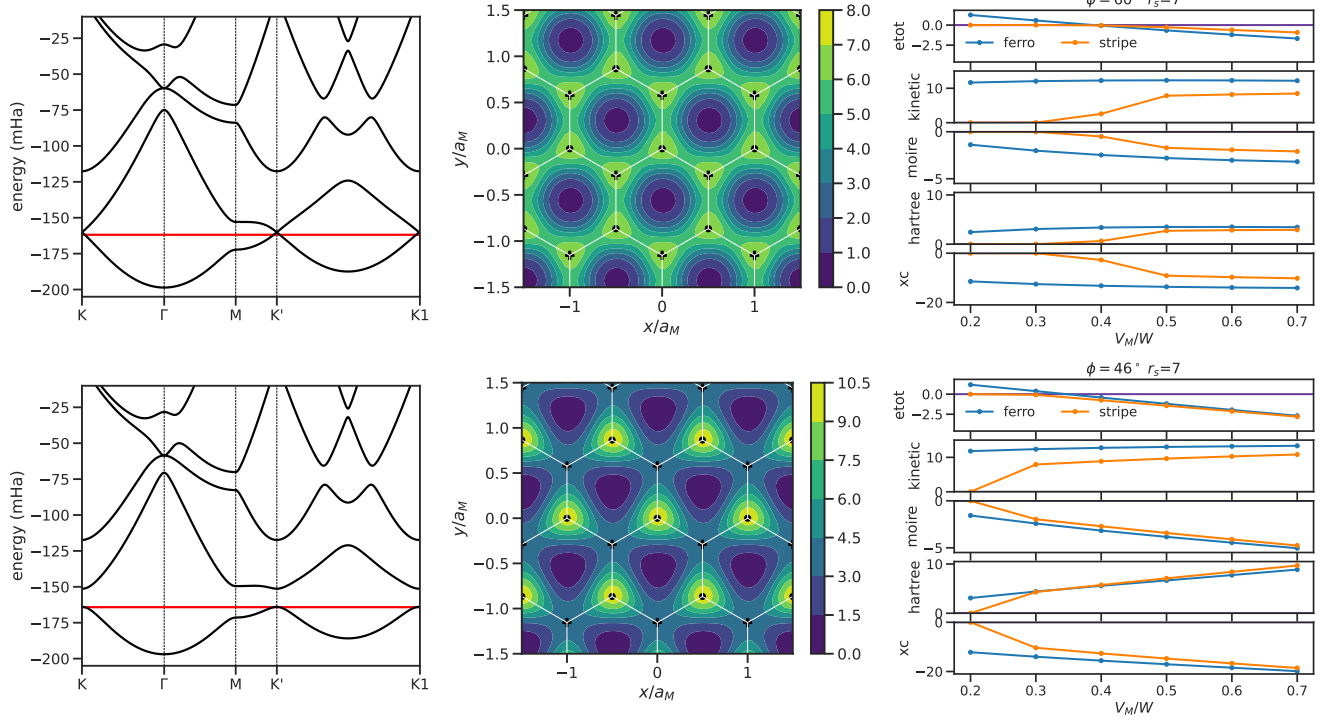


FIG. S4. LDA charge density (left panel) of the ferromagnetic state at $V_M/W = 0.5$ and the corresponding band structure (middle panel) in two moiré potentials, one in the honeycomb limit ($\phi = 60^\circ$ shown in the top row), while the other tuned towards the triangular limit, which is at $\phi = 0^\circ$. Black dots and crosses label the honeycomb A and B sublattices, respectively. Energy components (right column) of the FM phase is compared against those in a collinear phase with anti-ferromagnetic spin stripes, which is used as a proxy for the AFM phase.